NANO LETTERS

Letter

pubs.acs.org/NanoLett

Precise Perforation and Scalable Production of Si Particles from Low-Grade Sources for High-Performance Lithium Ion Battery Anodes

Linqi Zong, Yan Jin, Chang Liu, Bin Zhu, Xiaozhen Hu, Zhenda Lu, and Jia Zhu*

National Laboratory of Solid State Microstructures, College of Engineering and Applied Sciences and Collaborative Innovation Center of Advanced Microstructures, Nanjing University, Nanjing 210093, P. R. China

Supporting Information

ABSTRACT: Alloy anodes, particularly silicon, have been intensively pursued as one of the most promising anode materials for the next generation lithium-ion battery primarily because of high specific capacity (>4000 mAh/g) and elemental abundance. In the past decade, various nanostructures with porosity or void space designs have been demonstrated to be effective to accommodate large volume expansion (~300%) and to provide stable solid electrolyte interphase (SEI) during electrochemical cycling. However, how to produce these building blocks with precise morphology control at large scale and low cost remains a challenge. In addition, most of nanostructured silicon suffers from poor Coulombic efficiency due to a large surface area and Li ion trapping at the surface coating. Here we demonstrate a unique nanoperforation process, combining modified ball milling, annealing, and acid treating, to produce porous Si with precise and continuous porosity control (from 17% to 70%), directly from low cost metallurgical silicon source (99% purity, ~ $1/kg). The produced porous Si coated with graphene by simple ball milling can deliver a reversible specific capacity of 1250 mAh/g over 1000 cycles at the rate of 1C, with Coulombic efficiency of first cycle over 89.5%. The porous networks also provide efficient ion and electron pathways and therefore enable excellent rate performance of 880 mAh/g at the rate of 5C. Being able to produce particles with precise porosity control through scalable processes from low-grade materials, it is expected that this nanoperforation may play a role in the next generation lithium ion battery anodes, as well as many other potential applications such as optoelectronics and thermoelectrics.

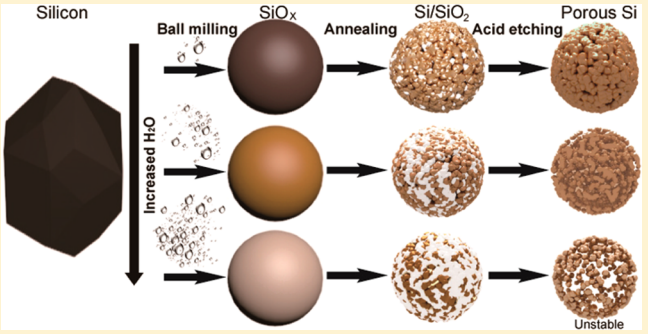

KEYWORDS: *Lithium battery, nanostructures, silicon, porous, low cost*

The emerging markets of portable electronics and electric vehicles generate tremendous demand for the development of advanced lithium-ion batteries (LIBs) with low cost, high energy, and power densities and a long cycling life.[1−24] Alloy anode materials such as Si, Ge, and Sn, while possessing high theoretical capacity,[25,26] also share common challenges related to large volume expansion during the lithiation and delithiation processes[27−30] and unstable solid-electrolyte interphase (SEI).[31−33] Recently, rational designed nanostructures with carefully tailored porosity or void space such as porous networks,[9,34−36] double-walled nanotubes,[37] yolk shell nanostructures,[38−42] and pomegranate-like structures[10] have been proposed to provide stable structures and interfaces despite the large volume expansion, therefore, leading to substantially improved cycling performance. However, to enable widespread applications, low cost and scalable processes are urgently needed to produce these building blocks with finely controlled porosity to enable high Coulombic efficiency, stable electrochemical cycling, and good rate performance.

Here we demonstrate a low-cost and scalable nanoperforation process, by combining modified ball milling, annealing, and acid treating, to produce porous Si particles with precise porosity control directly from low grade and low cost silicon sources. The porous silicon particles were produced essentially by three steps (Figure 1a) (see more details in Methods). First, a mixture of low grade silicon and water is ball-milled to produce silicon oxide (SiO_x) particles. As one of the key steps of the process, by controlling the initial ratio of silicon to water, SiO_x particles with oxygen content (x) ranging from 0.26 ($SiO_{0.26}$) to 1.93 ($SiO_{1.93}$) can be precisely tuned and massively produced (10 g per run in the lab). Table 1 lists the initial mole ratios of silicon to water added in and final mole ratios of silicon to oxygen in produced SiO_x particles examined by X-ray fluorescence (XRF), which confirms the direct correlation of these two. As demonstrated in Figure 1b, as the oxygen content increases (from $SiO_{0.26}$ to $SiO_{1.93}$), the color of produced SiO_x particles gradually changes, from black to yellow and to white eventually. As the sizes of these particles with different oxygen content remain unchanged (confirmed by dynamic light

Received: August 24, 2016
Revised: September 30, 2016
Published: October 5, 2016

DOI: 10.1021/acs.nanolett.6b03567
Nano Lett. 2016, 16, 7210−7215

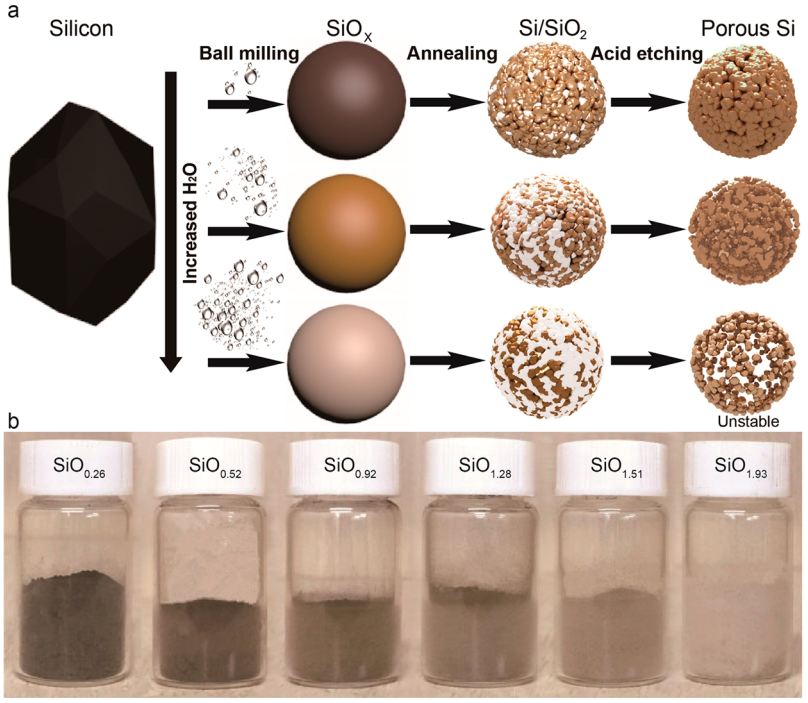

Figure 1. Nanoperforation processes: (a) Schematics of three steps: high energy mechanical milling (HEMM) with water, annealing, and acid etching. (b) Optical images of SiO_x particles after ball-milling with various oxygen contents.

Table 1. X-ray Fluorescence (XRF) Characterizations

Si:H_2O (mole ratio)	1:0.3	1:0.6	1:1	1:1.3	1:1.6	1:2
Si:O (mole ratio)	1:0.26	1:0.52	1:0.92	1:1.28	1:1.51	1:1.93

scattering, shown in Supplementary S1), the color difference is a direct indication of the composition difference.

These produced SiO_x particles are then heated to generate Si/SiO_2 composite because of the disproportionation of SiO_x.[43]

$$2SiO_x \rightarrow (2 - x)Si + xSiO_2$$

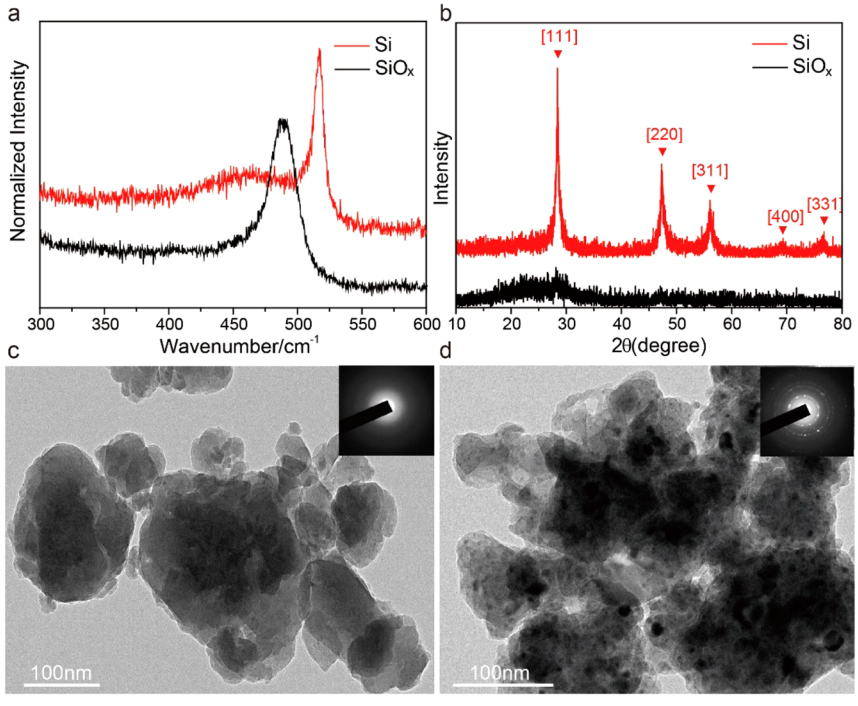

Figure 2. Characterizations of SiO_x particles: (a) Raman spectrum of produced SiO_x particles (water added) and Si particles (no water added), (b) XRD pattern of produced SiO_x particles (water added) and Si particles (no water added), (c) TEM image of SiO_x particles before annealing, (d) TEM image of Si/SiO_2 particles after annealing.

DOI: 10.1021/acs.nanolett.6b03567
Nano Lett. 2016, 16, 7210−7215

Table 2. Porosity Calculation and Measurement

porous Si	$SiO_{0.26}$	$SiO_{0.52}$	$SiO_{0.92}$	$SiO_{1.28}$	$SiO_{1.51}$	$SiO_{1.93}$
theoretical porosity	0.25	0.44	0.66	0.80	0.87	0.98
actual density (g/cm^3)	1.82	1.32	1.01	0.71	1.09	2.19
actual porosity	0.23	0.44	0.57	0.70	0.54	0.21
BET measurements (m^2/g)	19.2	49.4	175	254	152	41.0
BET measurements (m^2/g) (after graphene coating)	2.30	6.34	12.9	24.3	10.1	6.58

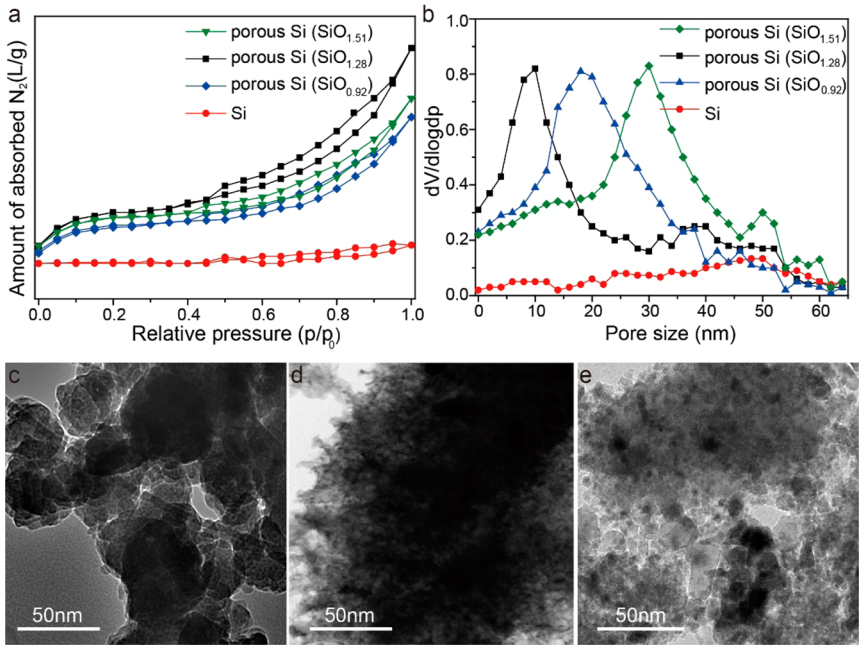

Figure 3. Characterizations of porous silicon from various SiO_x particles: (a) Nitrogen isotherm plots of different porous silicon particles made from $SiO_{0.92}$, $SiO_{1.28}$, and $SiO_{1.51}$, (b) pore volume distribution curves of different porous silicon particles made from $SiO_{0.92}$, $SiO_{1.28}$, and $SiO_{1.51}$, and (c, d, and e) TEM images of porous silicon made from $SiO_{0.92}$, $SiO_{1.28}$, and $SiO_{1.51}$, respectively.

It can be easily understood that SiO_x particles with various oxygen contents will result in Si/SiO_2 composites with different contents of SiO_2. With Si and SiO_2 uniformly distributed within each particle, once SiO_2 is removed by hydrofluoric (HF) acid treatment, a porous Si particle will be produced, as shown in Figure 1a.

To carefully examine the effect of water during ball milling, produced silicon oxide (water added) particles and silicon particles (no water added) are carefully examined by Raman spectroscopy (Figure 2a), which shows a clear difference, with the peak at 480 cm^{-1}, corresponding to the silicon oxide, and the peak of 510 cm^{-1} related to silicon. As shown in Figure 2b, the X-ray powder diffraction (XRD) pattern of SiO_x particles shows broad amorphous features and no peaks indicative of crystalline phases. In comparison, the diffraction peaks of silicon particles after ball milling (no water added) were sharp and intense, indicating their highly crystalline nature. The morphology and crystal quality of these produced SiO_x particles before and after thermal disproportionation are also carefully examined by transmission electron microscopy (TEM). Figure 2c shows a typical TEM image of SiO_x particles (~100 nm size) with homogeneous contrast and amorphous diffraction pattern. After thermal disproportionation, these particles become heterogeneous with mixed crystalline (Si) and amorphous (SiO_2) phases (Figure 2d). The crystal quality of Si in the composite after thermal disproportionation is clearly exhibited in a high-resolution TEM image (Figure S2 in Supporting Information).

Assuming Si and SiO_2 are uniformly distributed within each particle after thermal disproportionation, the porosity of produced porous silicon after HF etching can be estimated by calculating the volume fraction of SiO_2, which is listed as theoretical porosity in Table 2). As we explained in the previous section, as the initial water/silicon ratio increases, the contents of SiO_2 in the Si/SiO_2 composite after thermal disproportionation increases accordingly. However, it is found that the SiO_x particles with highest oxygen contents will not necessarily produce silicon particles with highest porosity. In fact, when the contents of SiO_2 in Si/SiO_2 composite are too high (as in the case of $SiO_{1.93}$), the remaining silicon contents will not be able to form stable porous networks (as shown in Figure 1a) but collapse to become smaller particles instead. Porosity can also be experimentally evaluated (listed as actual porosity in Table 2) by measuring the actual density of porous silicon (listed as actual density in Table 2), as compared to the density of bulk silicon. As shown in Table 2, when x is lower than 1.28, the actual porosity agreed well with the theoretical calculation. If the value of x continues to increase above 1.28, the porosity exhibits significant decrease, deviating from the theoretical calculation, which is expected for the reason mentioned above. It is found that $SiO_{1.28}$ particles can produce porous silicon with the highest porosity of 70% through this process.

This dependence of porosity on the oxygen contents of SiO_x is well-captured by Brunauer–Emmett–Teller (BET) nitrogen adsorption (Figure 3a) of porous silicon particles produced

DOI: 10.1021/acs.nanolett.6b03567
Nano Lett. 2016, 16, 7210–7215

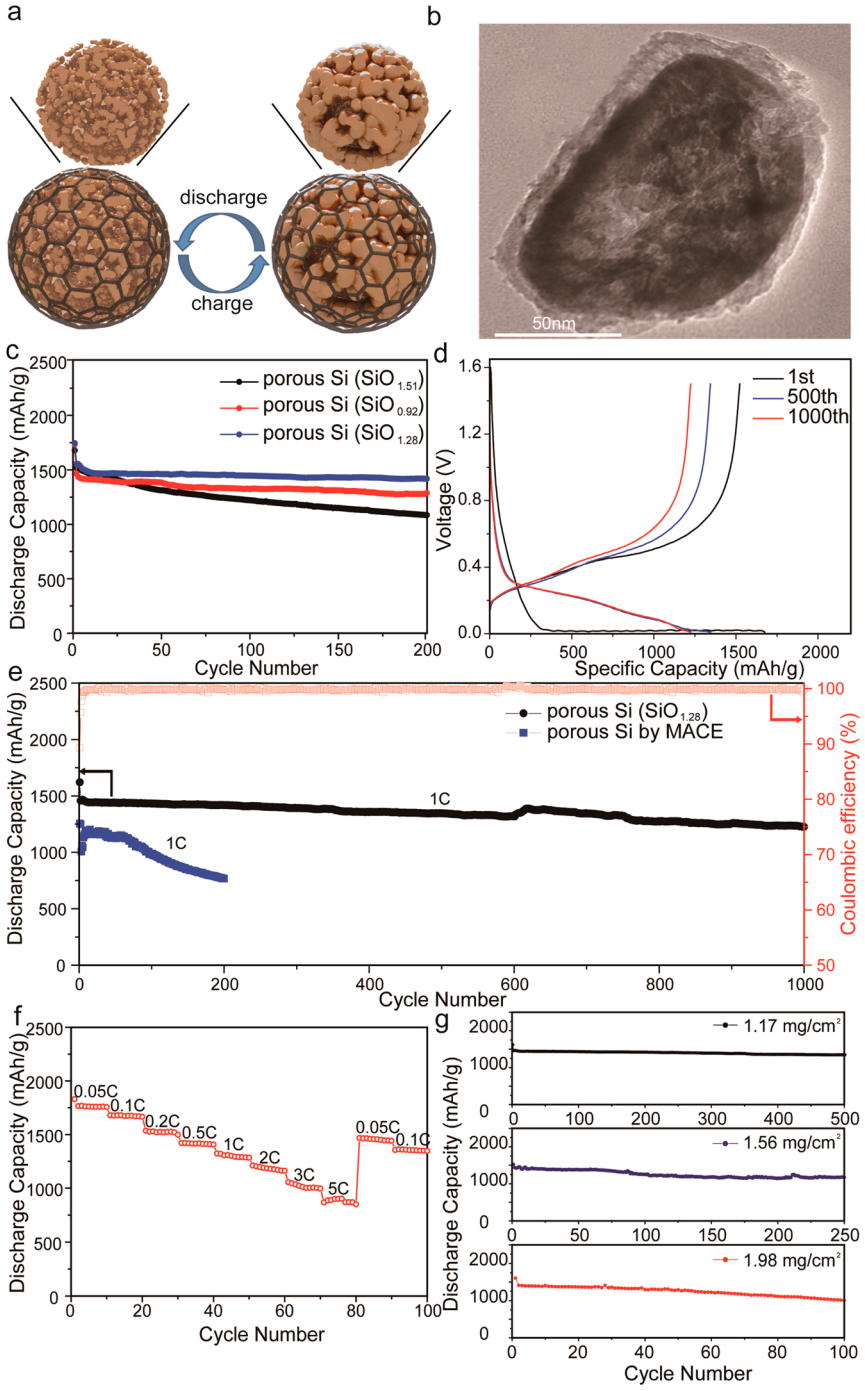

Figure 4. Electrochemical performanc: (a) Schematic of the charge/discharge process of Si/graphene composite, (b) TEM image of Si/graphene composite, (c) cycling performance of porous-Si/graphene composite with different porosity at a rate of 1 C, (d) voltage profiles for the porous-Si/graphene composite plotted for the 1st, 500th, and 1000th cycles, (e) discharge capacity and Coulombic efficiency (in red color) of porous-Si/graphene composite and discharge capacity of porous Si by MACE process, (f) cycling performance at different rates from 0.05 C to 5 C, (g) cycling performance of different areal mass loadings of the cell.

from $SiO_{0.92}$, $SiO_{1.28}$, and $SiO_{1.51}$. It is clear that the amount of adsorbed N_2 of porous Si (produced by $SiO_{1.28}$) is the highest. The BET surface area of that sample was calculated to be 175 $m^2\ g^{-1}$, which is the highest specific surface area among all samples listed in Table 2. The pore size distribution, derived from desorption data and calculated from the isotherm, shows that porous silicon from $SiO_{1.28}$ has the smallest pore sizes. Transmission electron microscopy (TEM) is used to carefully examine the morphologies of produced silicon particles from SiO_x with different oxygen contents ($SiO_{0.92}$, $SiO_{1.28}$, and $SiO_{1.51}$). As shown in Figure 3c, the TEM image of porous silicon particles from $SiO_{0.92}$ reveals its interconnected structures with a size of about 30 nm. For porous silicon particles from $SiO_{1.28}$, it turned into the clear porous structure (Figure 3d). As oxygen content further increases ($SiO_{1.5}$), the produced silicon particles have much smaller feature size of 5−10 nm.

DOI: 10.1021/acs.nanolett.6b03567
Nano Lett. 2016, 16, 7210−7215

As demonstrated above, based on nanoperforation process, we can produce Si particles with precise porosity control, ideal building blocks for advanced lithium ion battery anode. As an example of demonstration, we combine the porous silicon with graphene (10% weight of porous silicon) by simple ball-milling to form porous Si/graphene composite (Figure 4a). This structure offers several advantages: highly porous silicon will have a much reduced volume change,[9] while the graphene shell enhances the electrical conductivity and at the same time serves as a stable interface for stabilizing SEI formation.[44−46] In addition, different from amorphous carbon shell, the graphene shell will not trap the lithium ions which is therefore beneficial for Coulombic efficiency. Therefore, it is expected that porous Si/graphene composite can offer a high capacity, stable cycling performance, and good rate performance as well as high Coulombic efficiency. The TEM image (Figure 4b) shows a typical structure of porous Si/graphene composite, with a uniform layer of graphene (~5 nm) formed on the surface of porous silicon particles. Figure 4c demonstrates the cycling performance of porous silicon from $SiO_{0.92}$, $SiO_{1.28}$, and $SiO_{1.51}$ after graphene coating. It is clear that porous silicon produced by $SiO_{1.28}$ has the most stable cycling performance, which is expected as porous silicon with a higher porosity will have a reduced volume change during electrochemical cycling. As shown in Figure 4e, after 1000 deep cycles at a rate of 1 C, the capacity of porous silicon produced by $SiO_{1.28}$ still maintains above 1250 mA h/g, which corresponds to the capacity decay \ as small as 0.015% per cycle, much better compared to the porous silicon fabricated by commonly used metal-assisted chemical etching with the same porosity. Coulombic efficiency is an important indicator of the reversibility of the electrode reaction. With graphene coating, the initial Coulombic efficiency reached 89.5% which is higher than most of previous studies related to nano-Si anode without prelithiation treatment. The Coulombic efficiency quickly increases to 99.00% within the first five cycles and to 99.90% within ten cycles. The averaged Coulombic efficiency from 2nd to 1000th cycles of the graphene coated Si particles is 99.90%. The first lithiation potential shows a plateau between 0.1 and 0.01 V, consistent with the behavior of crystal Si (Figure 4d). As shown in Figure 4f, the capacity of porous Si/graphene composite varies from 1790 mA h/g to 880 mA h/g at charge/discharge rate from C/20 to 5 C. Stable cycling for over 100 cycles is demonstrated with areal mass loading as high as 1.98 mg cm^{-2} (Figure 4g). The volumetric capacity is about 1360 A h/L for the first cycle and 850 A h/L after 1000 cycles at a current rate of 1 C. Compared with graphite, our materials' volumetric capacity is more than three times higher than the common commercial graphite anodes, and gravimetric capacity is more than five times higher than the common commercial graphite anodes, which is a great step forward.

Based on ball milling, thermal disproportionation and acid treating, we demonstrate an ingenious and scalable nanoperforation process that can produce silicon directly from low grade sources with continuous and precise porosity control, which can serve as excellent building blocks for the construction of next generation energy storage devices. It also opens tremendous opportunities to recover low-quality materials for commercially viable materials, which can be generally applied to a variety of material systems and energy applications such as optoelectronics and thermoelectrics.[47−50]

Methods. *Procedures of the Nanoperforation Process.* Metallurgical silicon (around 99% purity) was used as received to prepare porous silicon particles via high energy mechanical mill (HEMM, Fritsch Planetary Micro Mill Pulverisette 7 premium line), annealing, and acid treatment. It was first crushed into millimeter range and then ball-milled with deionized water into particles by HEMM for 2 h at a speed of 1000 r/min with 3 mm grinding balls to achieve SiO_x particles. The oxygen contents of SiO_x particles depend on the amount of deionized water added. The SiO_x particles were directly heated to 1000 °C under Ar atmosphere. Then SiO_2 was removed with HF, followed by filtration and deionized water washing three times. The final porous silicon particles were obtained after drying in a vacuum oven.

MACE Process. The metallurgical silicon powder was immersed in a solution of 20 mM silver nitrate ($AgNO_3$) and 5 M hydrofluoric acid (HF) at 50 °C for 2 h. Then, DI water was substituted by 30 mL of ethanol and an additional 1 mL of H_2O_2 to get porous silicon. Silver (Ag) on the surface was then removed in concentrated nitric acid for 1 h.

Synthesis of Si/Graphene Composite. Graphene was first ball-milled for 30 min at a speed of 800 r/min with 3 mm grinding balls. Then porous silicon particles were added in followed by ball-milling for 2 h at a speed of 400 r/min to produce the Si/graphene composite.

Material Characterizations. The morphologies and structures of the as-prepared porous Si particles were characterized by scanning electron microscopy (Dual-beam FIB 235, FEI Strata) and transmission electron microscopy (JEM-200CX). XRD spectra were obtained on a Rigaku Ultima X-ray IV. Other characterizations were carried out by Raman spectroscopy (WITEC Raman spectrometer), NanoDLS (Brookhaven Instruments Corporation), UltraPYC 1200e, and BET (Autosorb-iQ).

Electrochemical Testing. Approximately 2 g of multiwall CNT was pretreated in 200 mL of HNO_3:H_2SO_4 = 3:1 (Mw) acid mixture at 90 °C for 1.5 h to well-dispersed CNT in aqueous solution. Filtration was conducted to separate MWCNT and acid before dispersing MWCNT back into 200 mL DI water. Then, dialysis was performed to neutralize MWCNT solution until pH reaches the range of 5−7. The concentration of as-obtained MWCNT was determined by evaporating a specific volume of solution and weighting the mass of MWCNT. ~8 wt % of MWCNT was mixed with Si/graphene composite. Then this productse are mixed with carbon black and CMC binder (80:5:15, weight ratio) to make slurry and then cast onto a thin copper foil and dried in a vacuum oven at 90 °C overnight and 110 °C for 2 h. Coin-type cells (2032) were fabricated inside an Ar-filled glovebox using Li metal foil as counter/reference electrode, along with a celgard 2250 separator. The electrolyte employed was 1.0 M $LiPF_6$ in 1:1 vol/vol ethylene carbonate/diethyl carbonate with 2 wt % vinylene carbonate (Guotai Huarong) added to improve the cycling stability. Galvanostatic cycling was performed using a LANHE CT2001A, the galvanostatic voltage cutoffs were 0.01 and 1.5 V vs Li/Li+. The charge/discharge rate was calculated with respect to the theoretical capacity of Si (4200 mA h/g, 1 C = 4200 mA/g). All of the capacities reported in the manuscript were based on the whole mass of the electrode (including active materials, binder, and acetylene black). The mass loading of each electrode was 1−2 mg/cm^2.

DOI: 10.1021/acs.nanolett.6b03567
Nano Lett. 2016, 16, 7210−7215

■ ASSOCIATED CONTENT

Supporting Information

The Supporting Information is available free of charge on the ACS Publications website at DOI: 10.1021/acs.nanolett.6b03567.

DLS test analysis of particles size after ball milling and acid etching, high resolution TEM image of porous silicon particles (PDF)

■ AUTHOR INFORMATION

Corresponding Author

*E-mail: jiazhu@nju.edu.cn (J.Z.).

Notes

The authors declare no competing financial interest.

■ ACKNOWLEDGMENTS

This work is jointly supported by the State Key Program for Basic Research of China (No. 2015CB659300), National Natural Science Foundation of China (NSFC No. 11321063 and No. 11574143) and the Natural Science Foundation of Jiangsu Province (No. BK20150056), the Priority Academic Program Development of Jiangsu Higher Education Institutions (PAPD) and the Fundamental Research Funds for the Central Universities.

■ REFERENCES

(1) Zong, L.; Zhu, B.; Lu, Z.; Tan, Y.; Jin, Y.; Liu, N.; Hu, Y.; Gu, S.; Zhu, J.; Cui, Y. *Proc. Natl. Acad. Sci. U. S. A.* **2015**, *112* (44), 13473−13477.

(2) Bruce, P. G.; Scrosati, B.; Tarascon, J. M. *Angew. Chem., Int. Ed.* **2008**, *47* (16), 2930−2946.

(3) Kim, H.; Han, B.; Choo, J.; Cho, J. *Angew. Chem.* **2008**, *120* (52), 10305−10308.

(4) Ji, X.; Lee, K. T.; Nazar, L. F. *Nat. Mater.* **2009**, *8* (6), 500−506.

(5) Park, M.-H.; Kim, M. G.; Joo, J.; Kim, K.; Kim, J.; Ahn, S.; Cui, Y.; Cho, J. *Nano Lett.* **2009**, *9* (11), 3844−3847.

(6) Magasinski, A.; Dixon, P.; Hertzberg, B.; Kvit, A.; Ayala, J.; Yushin, G. *Nat. Mater.* **2010**, *9* (4), 353−358.

(7) Su, Y.-S.; Manthiram, A. *Nat. Commun.* **2012**, *3*, 1166.

(8) Jung, D. S.; Ryou, M.-H.; Sung, Y. J.; Park, S. B.; Choi, J. W. *Proc. Natl. Acad. Sci. U. S. A.* **2013**, *110* (30), 12229−12234.

(9) Li, X.; Gu, M.; Hu, S.; Kennard, R.; Yan, P.; Chen, X.; Wang, C.; Sailor, M. J.; Zhang, J.-G.; Liu, J. *Nat. Commun.* **2014**, *5*, 4105.

(10) Liu, N.; Lu, Z.; Zhao, J.; McDowell, M. T.; Lee, H.-W.; Zhao, W.; Cui, Y. *Nat. Nanotechnol.* **2014**, *9* (3), 187−192.

(11) Su, X.; Wu, Q.; Li, J.; Xiao, X.; Lott, A.; Lu, W.; Sheldon, B. W.; Wu, J. *Adv. Energy Mater.* **2014**, *4* (1), 1300882.

(12) Zhao, Y.; Feng, J.; Liu, X.; Wang, F.; Wang, L.; Shi, C.; Huang, L.; Feng, X.; Chen, X.; Xu, L. *Nat. Commun.* **2014**, *5*, 4565.

(13) Li, Y.; Yan, K.; Lee, H.-W.; Lu, Z.; Liu, N.; Cui, Y. *Nature Energy* **2016**, *1*, 15029.

(14) Fu, Y.; Su, Y. S.; Manthiram, A. *Adv. Energy Mater.* **2014**, *4* (1), 1300655.

(15) Hu, Y. S.; Demir-Cakan, R.; Titirici, M. M.; Müller, J. O.; Schlögl, R.; Antonietti, M.; Maier, J. *Angew. Chem., Int. Ed.* **2008**, *47* (9), 1645−1649.

(16) Kim, M. G.; Cho, J. *Adv. Funct. Mater.* **2009**, *19* (10), 1497−1514.

(17) Wang, C.; Wu, H.; Chen, Z.; McDowell, M. T.; Cui, Y.; Bao, Z. *Nat. Chem.* **2013**, *5* (12), 1042−1048.

(18) Whittingham, M. S. *Chem. Rev.* **2004**, *104* (10), 4271−4302.

(19) Arico, A. S.; Bruce, P.; Scrosati, B.; Tarascon, J.-M.; Van Schalkwijk, W. *Nat. Mater.* **2005**, *4* (5), 366−377.

(20) Armand, M.; Tarascon, J.-M. *Nature* **2008**, *451* (7179), 652−657.

(21) Kang, B.; Ceder, G. *Nature* **2009**, *458* (7235), 190−193.

(22) Dunn, B.; Kamath, H.; Tarascon, J.-M. *Science* **2011**, *334* (6058), 928−935.

(23) Zhu, B.; Jin, Y.; Tan, Y.; Zong, L.; Hu, Y.; Chen, L.; Chen, Y.; Zhang, Q.; Zhu, J. *Nano Lett.* **2015**, *15* (9), 5750−5754.

(24) Jin, Y.; Zhang, S.; Zhu, B.; Tan, Y.; Hu, X.; Zong, L.; Zhu, J. *Nano Lett.* **2015**, *15* (11), 7742−7747.

(25) Park, C.-M.; Kim, J.-H.; Kim, H.; Sohn, H.-J. *Chem. Soc. Rev.* **2010**, *39* (8), 3115−3141.

(26) Zhang, W.-J. *J. Power Sources* **2011**, *196* (1), 13−24.

(27) Beaulieu, L.; Eberman, K.; Turner, R.; Krause, L.; Dahn, J. *Electrochem. Solid-State Lett.* **2001**, *4* (9), A137−A140.

(28) Obrovac, M.; Christensen, L. *Electrochem. Solid-State Lett.* **2004**, *7* (5), A93−A96.

(29) Obrovac, M.; Christensen, L.; Le, D. B.; Dahn, J. *J. Electrochem. Soc.* **2007**, *154* (9), A849−A855.

(30) Deshpande, R.; Cheng, Y.-T.; Verbrugge, M. W. *J. Power Sources* **2010**, *195* (15), 5081−5088.

(31) Aurbach, D. *J. Power Sources* **2000**, *89* (2), 206−218.

(32) Chan, C. K.; Ruffo, R.; Hong, S. S.; Cui, Y. *J. Power Sources* **2009**, *189* (2), 1132−1140.

(33) Verma, P.; Maire, P.; Novák, P. *Electrochim. Acta* **2010**, *55* (22), 6332−6341.

(34) Ge, M.; Rong, J.; Fang, X.; Zhou, C. *Nano Lett.* **2012**, *12* (5), 2318−2323.

(35) Du, F. H.; Li, B.; Fu, W.; Xiong, Y. J.; Wang, K. X.; Chen, J. S. *Adv. Mater.* **2014**, *26* (35), 6145−6150.

(36) Lu, Z.; Liu, N.; Lee, H.-W.; Zhao, J.; Li, W.; Li, Y.; Cui, Y. *ACS Nano* **2015**, *9* (3), 2540−2547.

(37) Wu, H.; Chan, G.; Choi, J. W.; Yao, Y.; McDowell, M. T.; Lee, S. W.; Jackson, A.; Yang, Y.; Hu, L.; Cui, Y. *Nat. Nanotechnol.* **2012**, *7* (5), 310−315.

(38) Liu, N.; Wu, H.; McDowell, M. T.; Yao, Y.; Wang, C.; Cui, Y. *Nano Lett.* **2012**, *12* (6), 3315−3321.

(39) Hong, Y. J.; Son, M. Y.; Kang, Y. C. *Adv. Mater.* **2013**, *25* (16), 2279−2283.

(40) Wang, B.; Li, X.; Zhang, X.; Luo, B.; Zhang, Y.; Zhi, L. *Adv. Mater.* **2013**, *25* (26), 3560−3565.

(41) Zhou, W.; Yu, Y.; Chen, H.; DiSalvo, F. J.; Abruña, H. c. D. *J. Am. Chem. Soc.* **2013**, *135* (44), 16736−16743.

(42) Li, S.; Niu, J.; Zhao, Y. C.; So, K. P.; Wang, C.; Wang, C. A.; Li, J. *Nat. Commun.* **2015**, *6*, 7872.

(43) Koyanagi, E.; Uchino, T. *Appl. Phys. Lett.* **2007**, *91* (4), 041910.

(44) Bunch, J. S.; Van Der Zande, A. M.; Verbridge, S. S.; Frank, I. W.; Tanenbaum, D. M.; Parpia, J. M.; Craighead, H. G.; McEuen, P. L. *Science* **2007**, *315* (5811), 490−493.

(45) Wu, J.; Pisula, W.; Müllen, K. *Chem. Rev.* **2007**, *107* (3), 718−747.

(46) Son, I. H.; Park, J. H.; Kwon, S.; Park, S.; Rümmeli, M. H.; Bachmatiuk, A.; Song, H. J.; Ku, J.; Choi, J. W.; Choi, J.-m. *Nat. Commun.* **2015**, *6*, 7393.

(47) Nayfeh, M. H.; Rao, S.; Barry, N.; Therrien, J.; Belomoin, G.; Smith, A.; Chaieb, S. *Appl. Phys. Lett.* **2002**, *80* (1), 121−123.

(48) Bera, C.; Mingo, N.; Volz, S. *Phys. Rev. Lett.* **2010**, *104* (11), 115502.

(49) Dai, F.; Zai, J.; Yi, R.; Gordin, M. L.; Sohn, H.; Chen, S.; Wang, D. *Nat. Commun.* **2014**, *5*, 3605.

(50) Yang, L.; Yang, N.; Li, B. *Nano Lett.* **2014**, *14* (4), 1734−1738.

DOI: 10.1021/acs.nanolett.6b03567
Nano Lett. 2016, 16, 7210−7215